



Research Paper

0D/2D interface engineering of carbon quantum dots modified Bi₂WO₆ ultrathin nanosheets with enhanced photoactivity for full spectrum light utilization and mechanism insight



Jiajia Wang^{a,b}, Lin Tang^{a,b,*}, Guangming Zeng^{a,b,*}, Yaocheng Deng^{a,b}, Haoran Dong^{a,b},
Yani Liu^{a,b}, Longlu Wang^c, Bo Peng^{a,b}, Chen Zhang^{a,b}, Fei Chen^{a,b}

^a College of Environmental Science and Engineering, Hunan University, Changsha, 410082, PR China

^b Key Laboratory of Environmental Biology and Pollution Control (Hunan University), Ministry of Education, Changsha 410082, PR China

^c State Key Laboratory of Chemo/Biosensing and Chemometrics, Hunan University, Changsha 410082, PR China

ARTICLE INFO

Keywords:

Carbon quantum dots
Bi₂WO₆
0D/2D heterojunction
Full spectrum light
Interface engineering
Density functional theory

ABSTRACT

A novel full spectrum light driven carbon quantum dots (CQDs)/Bi₂WO₆ (CBW) hybrid materials were synthesized via a facile hydrothermal method. Multiple techniques including XRD, TEM, XPS, BET, UV–vis, XPS, PL and TRPL, were employed to investigate the structures, morphology, optical and electronic properties and photocatalytic performance of as-prepared samples. The results indicated that CBW heterojunctions were assembled of CQDs on m-BWO and presented high separation efficiency of photo-generated carriers and full light spectrum absorption. The photocatalytic mechanism of CBW hybrid materials was revealed, suggesting that the excellent photocatalytic activity towards organic pollutants was ascribed to the up converted photoluminescence (PL) and electron reservoir properties of CQDs. Density functional theory calculations indicated that complementary conduction and valence band-edge hybridization between CQDs and m-BWO could apparently increase separation efficiency of electron-hole pairs of CBW hybrid materials. According to ESR measurement and quenching experiments, the O₂^{•−}, ·OH and h⁺ were the main active species during the photocatalytic process. This study could shed light on 0D/2D interface engineering of carbon quantum dots based heterojunctions with enhanced photoactivity for full spectrum light utilization in pollutant degradation and energy conversion.

1. Introduction

Inspired by the discovery of graphene in 2004, two-dimensional (2D) nanosheets with atomic thickness have attracted increasing interest due to their unique electronic structures and broad applications, particularly in catalysis [1–3]. As is known, ultrathin 2D nanosheets are considered as superior junction that could combine the microscopic structural features with outstanding macroscopic properties, realizing the maximum functionality with a minimized size [4,5]. Particularly, ultrathin 2D nanosheets have ultra-large specific surface area and unique surface structures and can be applied in series of research fields, such as catalysis, sensing, energy conversion, etc. For photocatalytic application, ultrathin 2D nanosheet materials enable the photo-generated carrier transfer from their inside to the surface, which results in high photoactivity [6]. Meanwhile, the ultrathin 2D nanosheets with large fraction of uncoordinated surface atoms could harvest more ultraviolet-visible light [7]. Therefore, it is desirable to fabricate ultrathin 2D nanosheets with a suitable band gap and apply them in

photocatalysis.

Bismuth tungstate (Bi₂WO₆), one of the most simple aurivillius oxides, has aroused much interest because of its low cost, high stability, nontoxicity and high photoactivity [8–10]. Bi₂WO₆ also consists of alternate stacking of [Bi₂O₂] layers and perovskite-type layers with oxygen atoms shared between layers [11–13]. Up to now, many strategies have been employed in order to acquire Bi₂WO₆ materials with high photocatalytic activity, such as morphology control [14,15], surface modification [16–18], and coupling with other photocatalysts [19,20]. Among them, the controllable preparation of atomic scale nanosheets may be an effective strategy. Recently, Zhou et al. fabricated monolayer Bi₂WO₆ nanosheets (m-BWO) with outstanding performance in solar energy conversion [21]. The ultrathin Bi₂WO₆ nanosheets could display improved separation efficiency of electron-hole pairs. However, the photo-activity of the pure Bi₂WO₆ materials is still not satisfactory due to its narrow photo-absorption from UV light to visible light regions which is shorter than 450 nm and the fast photo-generated electron-carriers recombination of single photocatalyst

* Corresponding authors at: College of Environmental Science and Engineering, Hunan University, Changsha, 410082, PR China.

E-mail addresses: tanglin@hnu.edu.cn (L. Tang), zgming@hnu.edu.cn (G. Zeng).

<http://dx.doi.org/10.1016/j.apcatb.2017.10.014>

Received 31 May 2017; Received in revised form 27 August 2017; Accepted 6 October 2017

Available online 08 October 2017

0926-3373/ © 2017 Elsevier B.V. All rights reserved.

semiconductor.

Carbon quantum dots (CQDs), as new class of 0D dimension carbon nanomaterials with size below 10 nm, can be amorphous or nanocrystalline with sp^2 carbon clusters and may fused with some sp^3 carbons with diamond-like structure [22,23]. Due to its unique properties, CQDs have shown tremendous potential as versatile nanomaterials utilized in bio-sensing, bio-imaging, chemical-sensing, drug-delivery, photodynamic therapy and electro-catalysis [24–26]. Recently, CQDs have been also introduced to photocatalytic applications due to the superior electron transfer ability. Notably, they possess both up and down-converted photoluminescence (PL), and electron-accepting and transport properties, which makes CQDs-based NIR light sensitive hybrid photocatalysts become promising agents for harvesting NIR light [27,28]. Several photocatalytic systems based on the CQDs have also been studied, such as CQDs/BiVO₄ [29,30], CQDs/TiO₂ [31,32], CQDs/g-C₃N₄ [33,34], CQDs/Cu₂O [35]. However, the relationships between 0D/2D interface engineering and photoactivity have not been systematically studied, and the insightful mechanism of photocatalysis by ultra-small CQDs based hybrid materials still needs to be further investigated. Considering the advantages of m-BWO and CQDs, the interface mismatch between the CQDs and m-BWO ultrathin nanosheets can be reduced, and nanoscale composites with intimate contacts can be constructed. This unique nanostructure are expected to have some advantages: a) the accessible area between the CQDs and m-BWO planar interface and the channels of bulk-to-surface for the electrons can be well structured; b) the enhanced utilization of the full spectrum of solar energy can be obtained; c) the ultra-small nanostructure can efficiently contact with contaminants, thus accelerating the interfacial charge transfer process; d) sp^2 carbon clusters of carbon quantum dots facilitate the adsorption capacity of nanostructure for organic pollutants, especially the hydrophobic pollutants. Inspired from the mentioned concepts, it is favorable to construct the architecture of ultrathin 2D nanosheets modified by CQDs to achieve efficient photocatalytic application for pollutant degradation and energy conversion.

In this work, a novel CQDs modified monolayer Bi₂WO₆ nanosheets (CBW) hybrid material was prepared via a hydrothermal method. The structures, morphologies, optical properties and photocatalytic properties were investigated in detail. Density functional theory (DFT) calculations were employed to reveal a strong interface interaction between CQDs and m-BWO. The photocatalytic activities of the as-prepared heterostructures were evaluated by the degradation of methylene orange (MO) and bisphenol A (BPA) which are toxic to human health under visible and near-infrared (IR) light irradiation [36,37]. It was demonstrated that CQDs modification was an effective approach to improve the photocatalytic performance. The present work could provide further insights into the effects of CQDs modifying m-BWO as well as the design of CQDs based heterojunctions with highly efficient full spectrum light driven activity for environmental applications.

2. Experimental

2.1. Synthesis of the photocatalysts

All the reagents were of analytical grade and were used without any further purification. The CQDs solid was fabricated according to Yang et al.'s previous work followed by the freeze-drying [38]. In general, a 5 mmol portion of citric acid was dissolved in 10 mL of deionized water and the 335 μ L ethylenediamine was added. The above solution was transferred into 25 mL Teflon-lined autoclave and heated at 200 °C for 5 h. After cooling to room temperature, the obtained product was subjected to dialysis for 12 h in order to get the purified CQDs solution. Then the CQDs solution was dealing with freeze-drying for 48 h to obtain the CQDs solid.

The CBW hybrid materials were synthesized via hydrothermal reaction. Typically, 1 mmol Na₂WO₄·2H₂O, and 2 mmol Bi(NO₃)₃·5H₂O and 0.05 g cetyltrimethylammonium bromide (CTAB) were added in

80 mL deionized water. After the mixture became clear, a certain amount of CQDs solid was added, and a brown solution appeared immediately. After magnetically stirring for 1 h, the mixed solution was transferred to a 100 mL Teflon-lined autoclave, and then sealed into a steel tank and heated to 120 °C for 24 h. Finally, the product was centrifugalized and washed several times with deionized water and vacuum dried at 60 °C for 12 h. The different mass ratio of CQDs/m-BWO at 1 wt%, 3 wt%, 5 wt%, and 7 wt% were prepared and were signed as CBW-1, CBW-3, CBW-5, and CBW-7, respectively. In contrast, pure m-BWO was prepared by the same procedure without adding CQDs.

2.2. Characterization

A Bruker XRD-D500 X-ray diffractometer (Cu K α source) was employed to record X-ray powder diffraction (XRD) patterns in the range from 5° to 80° at a scan rate of 8°/min. Transmission electron microscopy (TEM) images were obtained from a JEOL JEM-2100F transmission electron microscope at an accelerating voltage of 200 kV. X-ray photoelectron spectroscopy (XPS) measurement was performed on a VG Multi Lab 2000 system with a monochromatic Mg-K α source operated at 20 kV. FT-IR spectrum was performed on a Shimadzu FTIR spectrophotometer (IRAffinity-1) using KBr disks at room temperature. UV–vis diffuse reflection spectroscopy (DRS) was performed on a Cary 300 spectrophotometer using BaSO₄ as the reference. The nitrogen adsorption–desorption isotherms at 77 K were investigated using a Nova 2200 e Surface Area and Porosity Analyzer (Quantum, USA). The Raman spectrum of as-obtained sample was recorded on a Labram-010 Laser confocal Raman spectrometer at ambient temperature (about 25 °C). The photoluminescence (PL) measurements were carried out on fluorescence spectrophotometer (FluoroMax-4) at room temperature. Time-resolved photoluminescence (TRPL) decay spectra were measured on a FLS920 fluorescence spectrometer (Edinburgh Instrument). The electron spin resonance (ESR) signals of radicals spin-trapped by spin-trap reagent DMPO (Sigma Chemical Co.) in water were examined on a Bruker model ESR JES-FA200 spectrometer.

2.3. DFT calculations

All electronic structure calculations were performed within the framework of DFT by using the “Vienna ab initio simulation package” (VASP). The exchange-correlation interactions were treated within the spin-polarized generalized gradient approximation (GGA) by Perdew-Burke-Ernzerhof (PBE). The interaction between the ions and electrons was described using the projected augmented wave (PAW) formalism. For the 2D heterostructure, a vacuum layer thicker than 18 Å along the direction perpendicular to the surface was added to avoid the interactions between adjacent images. To get accurate results, the energy cutoff was set to 500 eV until the force on each atom was less than 0.01 eV/Å. A Gaussian smearing was used with a smearing width of 0.2 eV. The electronic structures were calculated with a basis set, consisting of the atomic orbitals of C, Bi, W, and O atoms with a $3 \times 3 \times 1$ k-mesh.

2.4. Photo-electrochemical measurements

CHI 660C electrochemical analyzer (CHI-660C, China) was used to measure the photo-electrochemical responses of the samples in a three-electrode cell. FTO electrodes deposited with samples served as the working electrode. A platinum foil served as counter and Ag/AgCl (3 M KCl) served as the reference electrodes. 0.1 M Na₂SO₄ was used as electrolyte solution. All the samples were analyzed without bias potential. The photo-responses of the samples as visible light switched on and off were measured at 0.0 V. A 300 W Xe lamp was chosen as a visible light and IR light source. All of the electrochemical measurements were carried out at room temperature.

2.5. Photocatalytic experiments

The photocatalytic activities were determined by the photo-degradation of MO and BPA under visible light and IR light irradiation of a 300 W xenon lamp (CEL-HXF300, Beijing AuLight). In each experiment, 100 mg of catalyst was suspended in an aqueous solution (100 mL) of MO and BPA in a quartz glass reactor. The initial concentrations of MO and BPA solutions were both 10 mg L⁻¹. Before photocatalytic reaction, the suspension was stirred in the dark for 60 min to reach the adsorption/desorption equilibrium. At given time intervals, 4 mL of the suspension was collected and then filtered through 0.45 µm membrane filters for analysis. The experimental temperature was kept at 25 °C. The concentration was analyzed by measuring the maximum absorbance using a Shimadzu UV-2100 spectrophotometer at 463 nm for MO. The concentration of BPA was analyzed by high performance liquid chromatography (HPLC, Agilent) equipped with a UV detector (SPD-10AV) and C₁₈ column (250 mm × 4.6 mm). The mobile phase was a mixture of 75/25 (v/v) acetonitrile-water mixture. The eluent was delivered at a rate of 1 mL·min⁻¹ and the wavelength for detection was 230 nm.

3. Results and discussion

3.1. Characterization

The crystal phase of pure m-BWO and CBW hybrid materials with different CQDs contents were measured by XRD. As shown in Fig. 1, the distinct diffraction peaks of samples locate at 28.3°, 32.8°, 47.1°, 56.0°, and 58.5° which correspond to the (1 3 1), (2 0 0), (2 0 2), (1 3 3), and (2 6 2) crystal planes of orthorhombic Bi₂WO₆ (JCPDS NO. 39-0256) [39], respectively. No other crystalline phase can be detected. The characteristic peak for carbon at 26° is too weak to be observed in CQDs/m-BWO hybrid materials, which is due to the low CQDs content in the samples [40].

The morphology and microstructure of the CQDs/m-BWO hybrid materials were characterized by transmission electron microscopy (TEM) and HRTEM analysis. The TEM image in Fig. 2a exhibits the synthesized m-BWO of a sheet shaped structure with the size ranging from 20 to 100 nm. The surface is smooth. HRTEM image are shown in Fig. 2b. As shown, the inter-planar spacing of 0.273 nm is clearly observed (inset of Fig. 2b) which corresponds to (200) crystallographic planes of Bi₂WO₆, in good agreement with the JCPDS card 39-0256 [41]. Fig. 2c shows the TEM image of CBW-3 particles, demonstrating sheets shaped structure morphology of m-BWO, and the introduction of CQDs to Bi₂WO₆ did not change the main morphology. Compared with pure m-BWO, a large number of CQDs with the diameter about 5–7 nm are evenly attached to the surface of Bi₂WO₆ nanosheets, which indicates that the CQDs have been coupled with Bi₂WO₆ successfully

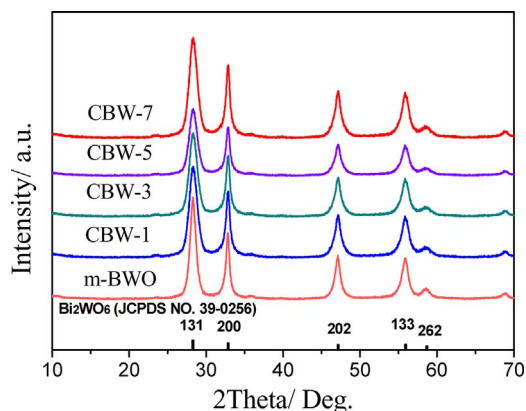


Fig. 1. XRD patterns of m-BWO and CBW hybrid materials.

(Fig. 2c). The HRTEM image in Fig. 2d also displays the lattice spacing of 0.32 nm (inset of Fig. 2d) which corresponds to the (002) spacing of graphitic carbon. The above results proved the successful formation of a CQDs/Bi₂WO₆ (CQDs size: ~5–7 nm) hybrid materials.

The chemical states of m-BWO and CBW-3 hybrid materials were investigated by X-ray photoelectron spectroscopy (XPS). Fig. 3a shows the survey scan XPS spectrum, which indicates that both m-BWO and CBW-3 are mainly composed of Bi, O, and W elements. Fig. 3b shows that binding energy peaks of Bi 4f_{5/2} and Bi 4f_{7/2} in m-BWO are located at 163.9 eV and 158.7 eV, respectively, implying the existence of Bi³⁺ in the crystal structure [42]. Compared with m-BWO, the Bi 4f peak in CBW-3 displays a slight shift about 0.2 eV toward higher binding energies due to the interaction between CQDs and m-BWO [43]. The O 1s peaks at 529.5 eV (Fig. 3c) can be assigned to the oxygen in Bi₂WO₆ crystals. The high-resolution W 4f XPS spectra of m-BWO and CBW-3 are shown in Fig. 3d. The binding energies of W 4f_{5/2} and W 4f_{7/2} are 37.2 eV and 35.0 eV in the oxide form of Bi₂WO₆, which can attributed to the W atoms existing in a +6 oxidation state [44]. For CBW-3, the binding energies of O 1s and W 4f also display more or less higher energy shift. Fig. 3e exhibits that the peak of the C1s could be de-convoluted into two peaks at 284.7 and 288.5 eV, which correspond to C–C sp²-hybridized carbon of CQDs and COO bond, respectively [45]. The result of XPS analysis indicated the coexistence of m-BWO and CQDs in the CQDs/m-BWO materials. In addition, the Raman spectra were obtained, as shown in Fig. S1. Two typical Raman bands were located at about 1309 and 1610 cm⁻¹ for CQDs, which corresponded to disordered sp³ carbon (D-band) and conjugated sp² (G-band) of carbon atoms, respectively. It is noticed that the G band of CBW-3 (1602 cm⁻¹) shifts toward lower wavelength, compared to that of CQDs (1610 cm⁻¹). The shift of the G band suggests that CQDs are chemically bonded to the m-BWO surface [41]. The Raman spectra also show that the I_D/I_G value of pure CQDs was higher than that of CBW-3, which is due to that the CQDs was reduced after hydrothermal hybridization with m-BWO.

To better understand the mechanism of interaction of the CQDs/m-BWO interface, it is insightful to investigate the interface electronic structures by DFT calculation. The electronic properties of the superlattice, such as the band structure VBM, CBM states, and charge difference density are calculated and shown in Fig. 4. Fig. 4a and b suggest that, after modifying CQDs on m-BWO, the charges were redistributed, which resulted in an electron-rich region on CQDs and a hole-rich region on m-BWO sheet. The charge difference density is also shown in Fig. 4c where green and dark yellow correspond to area with high density charge. The above results suggest that the formation of CQDs/m-BWO hybrid composite has significant effect on the electronic properties of CQDs and m-BWO sheet due to a strong interface interaction. The complementary conduction and valence band-edge hybridization between CQDs and m-BWO could lead to the spatial separation of electrons and holes, and reduce the recombination probability of charge carriers.

The specific surface area of the as-prepared samples was investigated using nitrogen adsorption-desorption analysis, and the results are shown in Fig. 5. Type IV isotherms are observed (inset of Fig. 5), indicating the existence of mesopores (2–50 nm) formed between m-BWO nanosheets. CBW-3 has higher pore volume than that of m-BWO. The BET specific surface areas and pore volumes of m-BWO and CBW-3 are summarized in Table S1. In comparison to pure m-BWO (42.6 m²·g⁻¹), the BET surface area of CBW-3 is higher (51.3 m²·g⁻¹). It should be noted that a higher BET surface area could provide more active sites and absorb more active species, thus leading to a higher photocatalytic activity.

3.2. Photoactivity test

The photoactivity of the as-prepared CQDs/m-BWO hybrid materials was investigated by the photodegradation of MO under visible

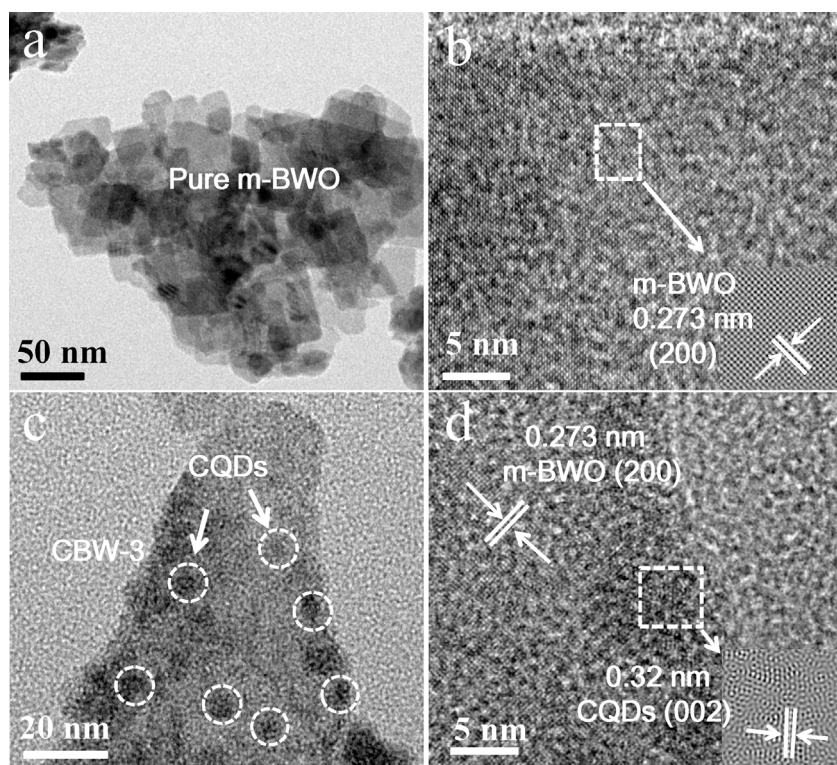


Fig. 2. TEM and HR-TEM images of m-BWO (a, b) and CBW-3 (c, d).

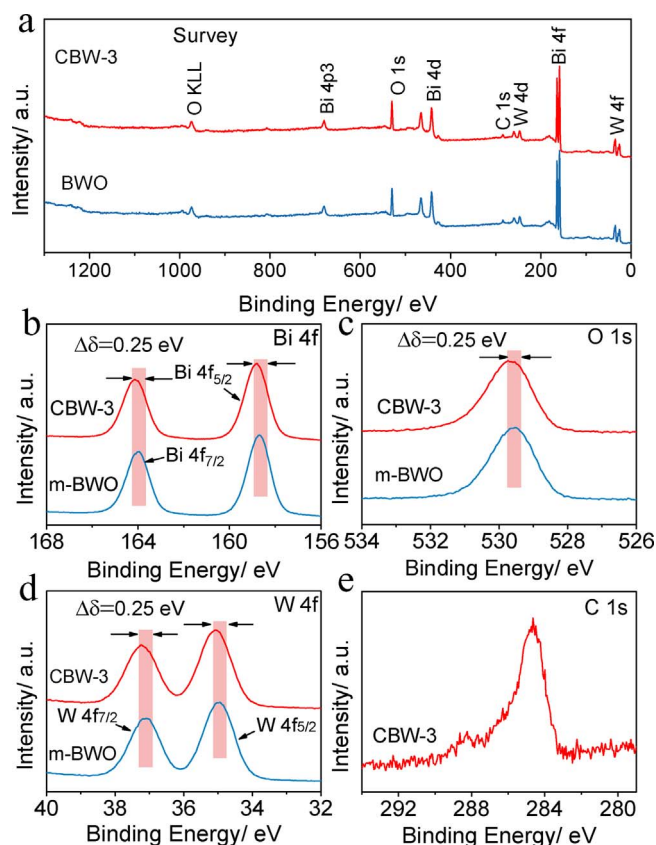


Fig. 3. XPS spectra of m-BWO and CBW-3: (a) survey spectrum; (b) Bi 4f spectrum; (c) O 1s spectrum; (d) W 4f spectrum; (e) C 1s spectrum.

light irradiation and IR light irradiation. Before the photodegradation process, the adsorption experiment of the CBW hybrid materials in the dark for the MO has been conducted (Fig. 6a). As shown in Fig. 6a, the

absorption of dye reached absorption equilibrium after 60 min. It can be seen that 10.6%, 12.3%, 16.5%, 20.2% and 25.6% of MO were adsorbed by m-BWO, CBW-1, CBW-3, CBW-5, and CBW-7 within 60 min, respectively. The absorption experiment demonstrated that CQDs decorated m-BWO hybrid materials facilitated the adsorption of MO because of π - π interaction [46]. As shown in Fig. 6b, 47.3% MO can be removed by m-BWO after 120 min irradiation. When the CQDs were introduced, the photocatalytic activity of the CBW hybrid materials was greatly enhanced. The CBW-3 displayed the highest photocatalytic activity, and the efficiency reached about 94.1%. When the CQDs content was higher than 3 wt%, the photocatalytic activity of the CBW hybrid materials decreased. Although the modification of CQDs to m-BWO facilitated the charge transfer from m-BWO to CQDs, but too many CQDs shadow the m-BWO surface from the incident visible light photons, leading to poor light exposure of m-BWO for photogenerated charge carrier generation [47,48]. The photocatalytic degradation kinetics of MO under visible light irradiation was investigated, and it was found that the changes of MO concentration versus the reaction time over CBW hybrid materials followed pseudo-first-order kinetics plot by the equation of $-\ln(C/C_0) = kt$, where t , C_0 , and C are the reaction time, initial MO concentration (mg/L), MO concentration at time t (mg/L); k represents the apparent pseudo-first-order rate constant (min^{-1}). Fig. 6c shows that CBW-3 has the maximum rate constant of 0.0190 min^{-1} , which is about 3 times higher than that of pure m-BWO (0.005 min^{-1}).

BPA, an endocrine disrupting chemical, may lead to various adverse effects on aquatic organisms even at low exposure levels [49]. The CBW hybrid materials have been used to explore the BPA removal under visible light irradiation. Fig. 6d shows that CQDs also facilitated the CBW adsorption of BPA. With increasing the proportion of CQDs, CBW-7 had the highest adsorption efficiency of BPA which could reach 58% after 1 h adsorption. As shown in Fig. 6e, 32.3% of BPA could be degraded over pure m-BWO under visible light irradiation for 60 min. After the introduction of CQDs, the CBW hybrid materials displayed a higher activity for the degradation of BPA than that of pure m-BWO, and CBW-3 also showed the highest photodegradation efficiency

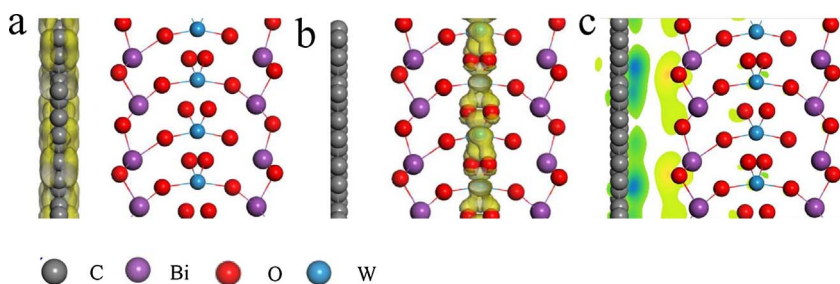


Fig. 4. The side view of the spatial distributions of partial charge densities of the VBM (a) and CBM (b) states for CBW-3; (c) deformation charge density for CBW-3. (For interpretation of the references to colour in this figure legend, the reader is referred to the web version of this article.)

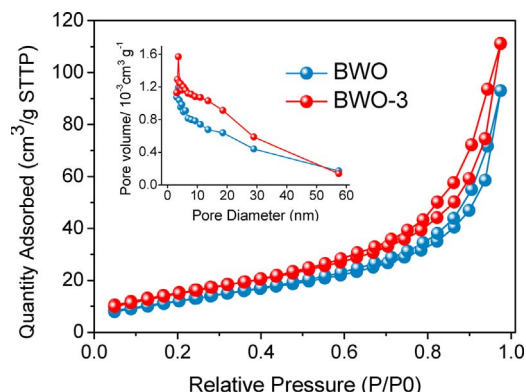


Fig. 5. N_2 adsorption-desorption isotherm of m-BWO and CBW-3.

towards BPA which could reach about 99.5% after 60 min irradiation. The detailed degradation process of BPA in the presence of CBW-3 is shown in Fig. S2. The photocatalytic degradation kinetics of BPA under visible light irradiation also followed pseudo-first-order kinetics plot. Fig. 6f shows that the rate constant for CBW-3 is 5 times as high as that of pure m-BWO, which indicates that CBW hybrid materials could be an efficient photocatalyst for photocatalytic removal of BPA in wastewater.

The photocatalytic performance of m-BWO and CBW-3 was further explored under IR light irradiation. As shown in Fig. 7a, only 8.5% MO can be photodegraded by m-BWO after 90 min under IR light

irradiation. After the modification of CQDs, the photocatalytic activity was significantly enhanced and 18.3% MO was photodegraded by CBW-3 under the same condition. CBW-3 has a rate constant of 0.0017 min^{-1} which is about 2.5 times higher than that of pure m-BWO (0.0064 min^{-1}) (in set of Fig. 7a). Fig. 7b shows that CBW-3 also exhibited higher activity than m-BWO for degradation of BPA under IR light irradiation. The photodegradation efficiency of CBW-3 reached 25.5% toward BPA which is 13.1% higher than that of m-BWO after 90 min under IR light irradiation. CBW-3 has a rate constant of 0.0027 min^{-1} which is about 1.5 times higher than that of pure m-BWO (0.0015 min^{-1}) (in set of Fig. 7b). The above results indicated that the CQDs played an important role for the enhancement of photocatalytic performance under the irradiation of IR light irradiation.

Three-dimensional (3D) EMMs (excitation-emission matrix fluorescence spectra) were employed to characterize the residual BPA solution during the photocatalytic process. 3D EMMs has been widely used as a rapid, selective and sensitive technology to study the physic-chemical properties of extracellular polymeric substances during the sludge hydrolysis processes, since their characteristics are closely correlated with the structure and functional groups in molecules [50]. Four samples were collected after adsorption equilibrium and at different visible light irradiation time intervals of 0 min, 20 min, and 120 min by CBW-3. As shown in Fig. 8a, the peak of BPA location (Peaks A) is identified at the excitation/emission wavelengths (Ex/Em) of 275–300/300–325 nm. According to the 3D EEMs contour plots in Fig. 8b, without irradiation, the BPA solution only contains one peak. Under visible light irradiation, a new peak (Peak B) at Ex/Em = 320–360/360–450 nm appeared at 20 min. The peak B at $\lambda_{\text{ex}}/\lambda_{\text{em}} = 320\text{--}360/360\text{--}450 \text{ nm}$ may be

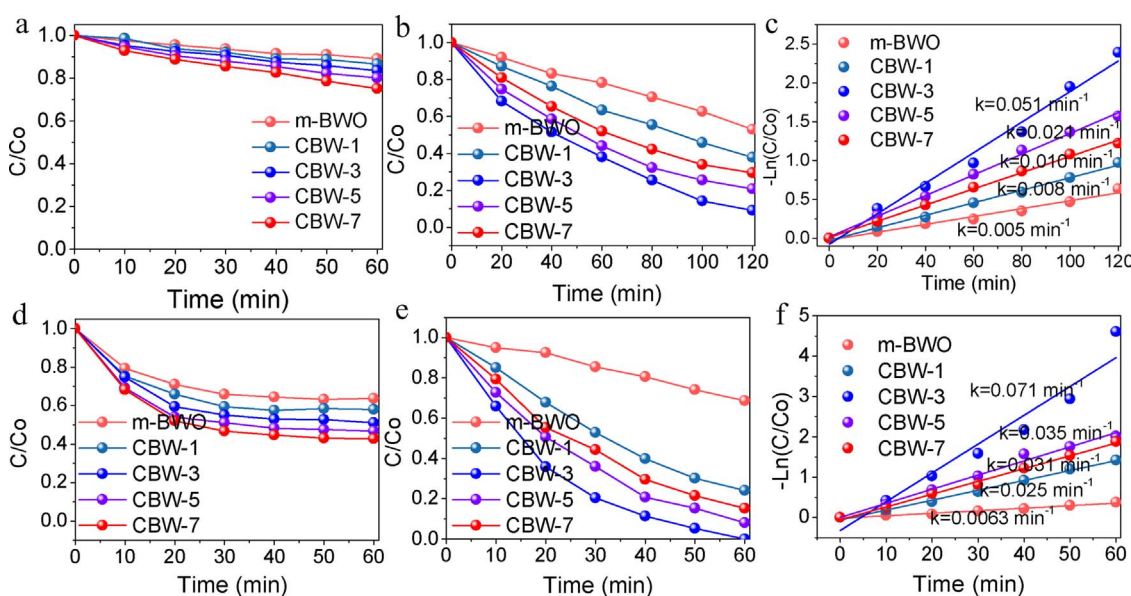


Fig. 6. (a) adsorption of MO by using pure m-BWO and CBW hybrid materials; (b) Photodegradation of MO by using pure m-BWO and CBW hybrid materials under visible light irradiation ($[MO] = 10 \text{ mg L}^{-1}$; $[CBW] = 1 \text{ g L}^{-1}$); (c) Plots of $\ln(C/C_0)$ vs irradiation time ($[MO] = 10 \text{ mg L}^{-1}$; $[CBW-3] = 1 \text{ g L}^{-1}$); (d) adsorption of BPA by using pure m-BWO and CBW hybrid materials; (e) Photodegradation of BPA by using pure m-BWO, and CBW hybrid materials under visible light irradiation ($[BPA] = 10 \text{ mg L}^{-1}$; $[CBW] = 1 \text{ g L}^{-1}$); (f) Plots of $\ln(C/C_0)$ vs irradiation time ($[BPA] = 10 \text{ mg L}^{-1}$; $[CBW-3] = 1 \text{ g L}^{-1}$).

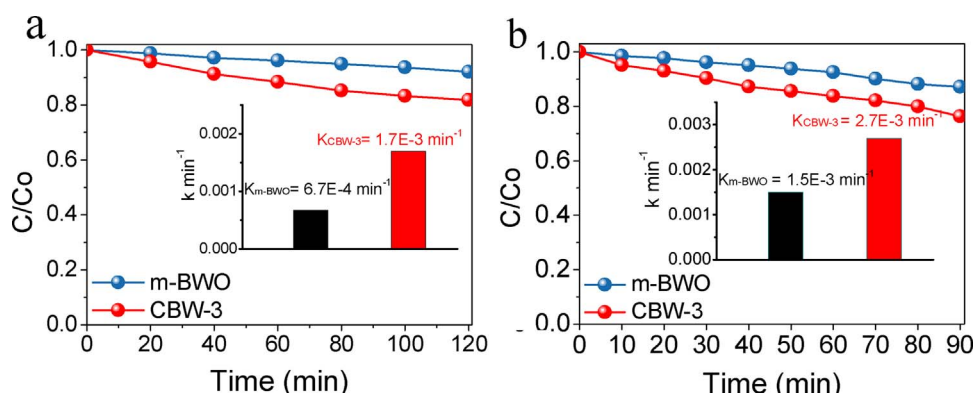


Fig. 7. (a) Photodegradation of MO by using pure m-BWO and CBW-3 under near-infrared light irradiation; (b) Photodegradation of BPA by using pure m-BWO and CBW-3 under near-infrared light irradiation. [MO, BPA] = 10 mg L^{-1} ; [CBW] = 1 g L^{-1} .

ascribed to humic acids-like fluorescence region [51–53]. The density (height) of peak A changed within the 20 min (Fig. 8c), which was attributed to photo-transformation intermediates, such as hydroxy derivatives. The change of fluorescence peaks is presumably because of the ring cleavage reaction. With the prolonged irradiation time (120 min), the density of peak A decreased, and the density of peak B increased (Fig. 8d). Furthermore, fluorescence parameters (including peak location, maximum intensity, and peak intensity) of the residue solution after 20 min and 120 min irradiation have been extracted from 3D EEMs, and are listed in Table S2. For peak A, the peak intensity decreases from 1542 to 749.5, suggesting the decreased BPA with the increase of irradiation time. However, the increased peak intensity for peak B from 260.5 to 518.5 has been obtained, implying the formation of humic acids-like substances.

The reusability and stability of the photocatalyst are vital to the practical application. To evaluate the reusability and stability of the CBW hybrid materials, recycling reactions are performed for photodegradation of BPA over CBW-3 hybrid material under visible light irradiation. After four consecutive cycles, no apparent deactivation of the

photocatalysts is observed, which implies the high stability of CBW hybrid materials (Fig. S3).

3.3. Investigation on optical and charge separation properties

The optical property of pure m-BWO and the CQDs/m-BWO hybrid materials were analyzed by UV–vis diffuse reflectance, and Fig. 9a shows that the pure m-BWO exhibited the absorption of sunlight with wavelength shorter than 450 nm, which is in accordance with previous report [21]. This absorption can be attributed to the charge transfer from the valence band to the conduction band of Bi_2WO_6 . Compared with pure m-BWO, CQDs/m-BWO hybrid materials display strong absorption in the range of 450–800 nm, indicating that the hybrid materials might have higher photoactivity, and CQDs played via roles in enhanced of sunlight absorption. Fig. 9b shows the steady-state PL spectra of pure m-BWO and CBW hybrid materials. The higher PL intensity means the higher recombination possibility of photo-generated electron-hole pairs [54]. As shown in Fig. 9b, all samples exhibit strong emission peak centered at around 420 nm and a shoulder at 460 nm.

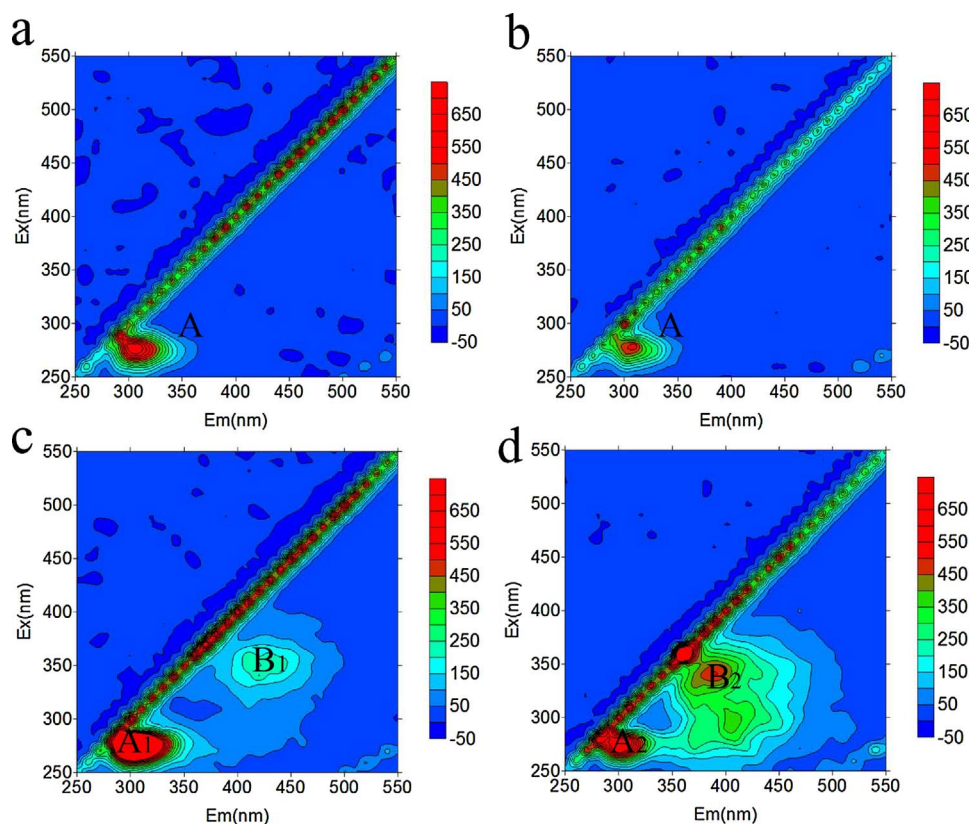


Fig. 8. 3D EEMs of the aqueous solution (a) taken from the original solution; (b) collected after 30 min adsorption in dark; (c) obtained after irradiation time of 20; and (d) obtained after irradiation time of 120, respectively. [BPA] = 10 mg L^{-1} ; [CBW-3] = 1 g L^{-1} .

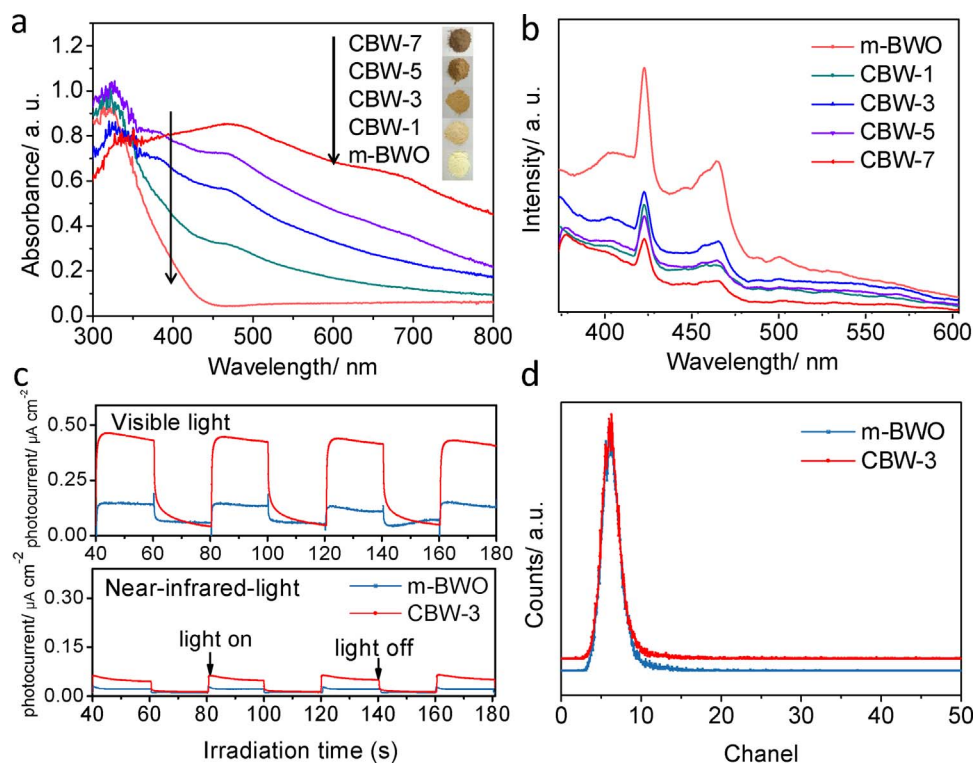


Fig. 9. (a) UV-vis spectra of m-BWO and CBW hybrid materials, inset: color change of CBW hybrid materials; (b) PL spectra of m-BWO and CBW hybrid materials; (c) Transient photocurrent response of m-BWO and CBW-3 under visible light and IR light irradiation, respectively; (d) TRPL decay spectra of m-BWO and CBW-3.

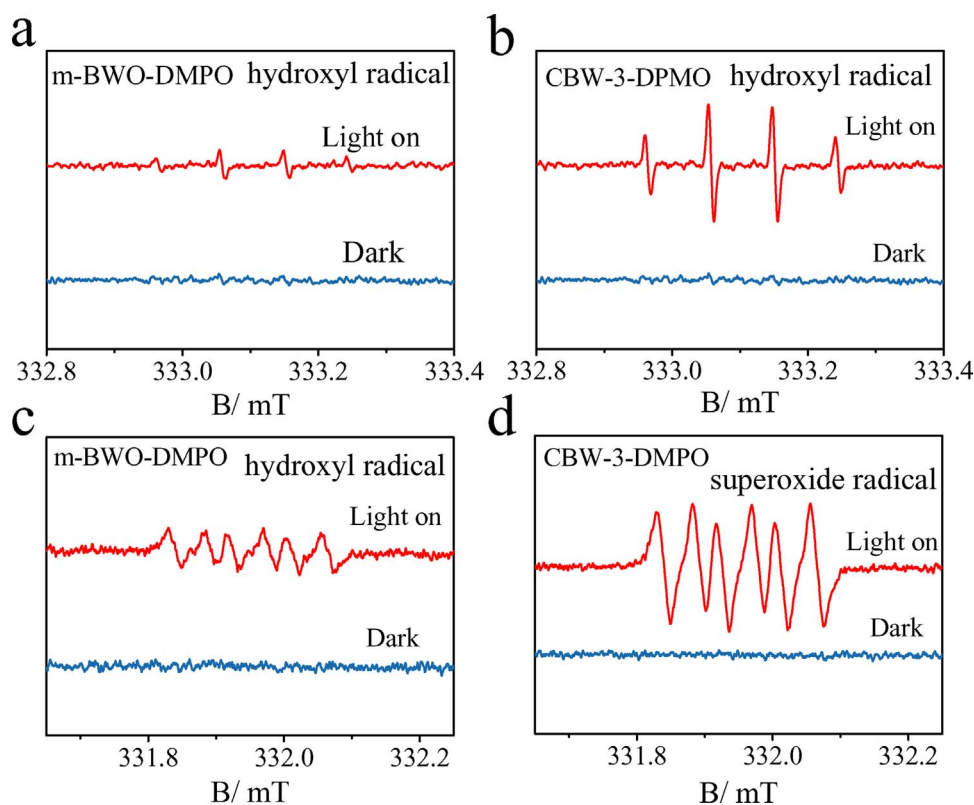


Fig. 10. ESR spectra of radical adducts trapped by DMPO (OH and O_2^-) in m-BWO and CBW-3 dispersion in the dark and under visible light irradiation in methanol dispersion for (a, b) DMPO- OH and (c, d) in aqueous dispersion for DMPO- O_2^- .

When CQDs was adhered to the Bi_2WO_6 surface, the intensity of centered peak band decreased apparently, suggesting efficient transfer of photo-generated electrons from Bi_2WO_6 to CQDs. The above results further demonstrated that the CBW hybrid materials have a higher separation rate of photoinduced electrons and holes.

It is believed that the introduction of CQDs not only helps the CBW improve the utilization of full spectrum light irradiation, but reduces

the electrons and holes recombination rate, which favors the effective charge separation of Bi_2WO_6 , thus improving the photocatalytic activities. To further prove this assumption, photocurrent-time ($I-t$) curves of CBW hybrid materials were performed under visible light irradiation and full near infrared light irradiation. It can be observed from Fig. 9c that CBW-3 has higher photocurrent response than that of the pure Bi_2WO_6 . It indicated that the CBW hybrid materials have a higher

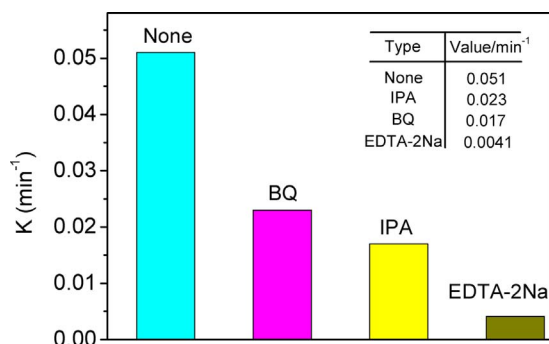


Fig. 11. Photodegradation efficiency of BPA on CBW-3 by addition of 2 mM benzoquinone, 10 mM isopropanol, 10 mM EDTA-Na₂. [BPA] = 10 mg L⁻¹; [CBW-3] = 1 g L⁻¹.

separation rate of photogenerated electrons and holes under visible light and near infrared light irradiation. It could be attributed to the fact that CQDs can convert near infrared light to visible light, thus improving the utilization of full spectrum light. Fig. S4 shows the PL spectra (350–750 nm) of CQDs excited by long wavelength light at 800, 900, 1000, and 1100 nm. It can be found that the emissions are located at shorter wavelengths of 520–600 nm. CQDs show a clear up-converted PL feature. In addition, the photo-generated electrons are excited from the VB to the CB of m-BWO and then transfer to CQDs, inhibiting the direct recombination of electrons and holes. Fig. 9d shows the comparison of TRPL decay spectra of m-BWO and CBW-3 composite. It is noted that the CBW-3 composite has a longer average decay time than that of pure m-BWO, suggesting that the formed heterojunction interface between CQDs and m-BWO can speed up photo-generated charges transfer, and effectively depress the charge recombination [55]. The above results strongly demonstrated that CBW hybrid materials have great potentiality in photocatalytic removal of pollutants in the full spectrum light.

3.4. Photocatalytic mechanism

ESR spin-trap technique was employed to study the main species generated by m-BWO and CBW-3 hybrid materials during the photodegradation process. Fig. 10a and b shows that the $\cdot\text{OH}$ radicals signal is not obvious for pure m-BWO under visible light irradiation, which is accordance with our previously report for Bi₂WO₆ samples [56]. However, for CBW-3 hybrid materials, the $\cdot\text{OH}$ radicals signal is stronger, suggesting the superior activity of the CBW hybrid materials for the photocatalytic degradation. In addition, the photoinduced electrons are excited in the middle layer and then they transfer to the edge of monolayers for reduction reactions. Fig. 10c and d shows that the reduction activity of CBW-3 hybrid material for O₂–O₂^{•-} is also enhanced, which enhanced the photoactivity of CBW hybrid materials.

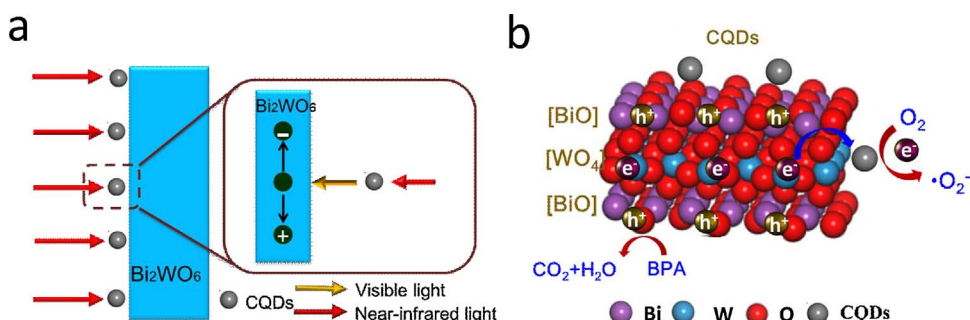
To investigate the roles of the active oxygen species on the photocatalytic process over CBW-3 hybrid materials, radicals trapping experiments are conducted. As shown Fig. 11, when the EDTA-2Na (quencher of h⁺) was added [57], it greatly inhibited the photocatalytic

degradation of MO, which indicates that the h⁺ plays the important role in the photocatalysis process. When the *p*-benzoquinone (BQ) and isopropyl alcohol (IPA) was added (IPA for $\cdot\text{OH}$ and BQ for O₂^{•-}) [58] separately, the photodegradation efficiency was also obviously affected, which indicates that the $\cdot\text{OH}$ and O₂^{•-} were also the main active species. The ESR analysis and free radicals trapping experiments indicated that $\cdot\text{OH}$, O₂^{•-} and h⁺ are the main active species.

Based on the above results, the enhanced photocatalytic activity of the CBW hybrid materials can be explained as follows. Firstly, CQDs can absorb near-infrared light, and then emit shorter wavelength light (400–750 nm) resulting in up conversion, which in turn excites m-BWO to form electron/hole pairs (as shown in Scheme 1a). Thus, CBW hybrid materials can effectively absorb the full spectrum of sunlight as a result of the enhanced photoactivities. Secondly, CQDs can act as an electron reservoir to trap electrons emitted from m-BWO particles due to irradiation by visible light, thus inhibiting the electron/hole pair recombination probability in the CBW hybrid materials (as shown in Scheme 1b). The e⁻ can accumulate at a higher energy level in ultrathin monolayer semiconductors [21]. Therefore, the excited electron can migrate from the CB of Bi₂WO₆ to the CQDs LUMO. O₂^{•-} radicals would be formed by the combination of electrons with O₂ adsorbed on the surfaces of CQDs, which leads to the degradation of BPA. The holes (h⁺) generated from VB band of m-BWO oxidize H₂O to form $\cdot\text{OH}$ radicals, then $\cdot\text{OH}$ radicals oxidize MO. In addition, h⁺ can directly oxidize BPA. These above aspects together account for the enhanced photocatalytic activity of CBW hybrid materials compared to pure m-BWO particles. It should be noted that CQDs with excellent up-converted PL and photoinduced electron transfer properties may provide a new approach to high-efficiency photocatalyst design for applications in energy technology.

4. Conclusion

In conclusion, we have successfully fabricated CBW hybrid materials via a facile hydrothermal process. According to the characterization of the structures, morphologies, optical and electronic properties, the hybrid material was formed with CQDs attached on the surface of Bi₂WO₆ monolayer nanosheet. Significantly, compared with pure m-BWO particles, CBW hybrid materials displayed enhanced photocatalytic activity for MO and BPA degradation under the visible light and IR light irradiation. The CBW-3 hybrid material exhibited the optimal photocatalytic performance. The excellent photocatalytic activity was ascribed to the up converted PL and electron reservoir properties of CQDs. DFT calculations indicated that complementary conduction and valence band-edge hybridization between CQDs and m-BWO could apparently increase separation efficiency of electron-hole pairs of CBW hybrid materials. According to ESR measurement and quenching experiments, the O₂^{•-}, $\cdot\text{OH}$ and h⁺ were the main active species during the photocatalysis process. 3D-EEM analysis showed that the by-products during the photocatalytic degradation of BPA by CBW were mainly humic acids-like substances. This study could shed light on 0D/2D interface engineering of carbon quantum dots based heterojunctions with enhanced photoactivity for full spectrum light utilization in



Scheme 1. (a) schematic diagram for up converted PL of CBW heterojunctions; (b) Photocatalytic mechanism scheme of CBW heterojunctions under visible and IR light irradiation (> 420 nm).

environmental applications.

Acknowledgements

The study was financially supported by Projects 51579096, 51521006, 51222805, 51679084, 51508175 and 51409024 supported by National Natural Science Foundation of China, the National Program for Support of Top-Notch Young Professionals of China (2012), and the Program for New Century Excellent Talents in University from the Ministry of Education of China (NCET-11-0129).

References

- [1] K.S. J. Novoselov, A.K. Geim, S.V. Morozov, D. Jiang, Y. Zhang, S.V. Dubonos, I.V. Grigorieva, A.A. Firsov, *Science* 306 (2004) 666–669.
- [2] G. Zeng, M. Chen, Z. Zeng, *Science* 340 (2013) 1403.
- [3] F. Chen, Q. Yang, S. Wang, F. Yao, J. Sun, Y. Wang, C. Zhang, X. Li, C. Niu, D. Wang, *Appl. Catal. B: Environ.* 209 (2017) 493–505.
- [4] L. Xu, J. Sun, *Adv. Energy Mater.* 6 (2016) 1600441.
- [5] Y. Sun, S. Gao, F. Lei, C. Xiao, Y. Xie, *Acc. Chem. Res.* 48 (2015) 3–12.
- [6] J. Li, G.M. Zhan, Y. Yu, L.Z. Zhang, *Nat. Commun.* 7 (2016).
- [7] Y.F. Sun, Z.H. Sun, S. Gao, H. Cheng, Q.H. Liu, J.Y. Piao, T. Yao, C.Z. Wu, S.L. Hu, S.Q. Wei, Y. Xie, *Nat. Commun.* 3 (2012) 7.
- [8] J. Wu, F. Duan, Y. Zheng, Y. Xie, *J. Phys. Chem. C* 111 (2007) 12866–12871.
- [9] C. Zhang, Y. Zhu, *Chem. Mater.* 17 (2005) 3537–3545.
- [10] D.L. Huang, G.-M. Zeng, C.L. Feng, S. Hu, X.-Y. Jiang, L. Tang, F.-F. Su, Y. Zhang, W. Zeng, H.-L. Liu, *Environ. Sci. Technol.* 42 (2008) 4946–4951.
- [11] L. Tang, J. Wang, G. Zeng, Y. Liu, Y. Deng, Y. Zhou, J. Tang, J. Wang, Z. Guo, J. Hazard. Mater. 306 (2016) 295–304.
- [12] J. Tang, Z. Zou, J. Ye, *Catal. Lett.* 92 (2004) 53–56.
- [13] P. Xu, G.M. Zeng, D.L. Huang, C.L. Feng, S. Hu, M.H. Zhao, C. Lai, Z. Wei, C. Huang, G.X. Xie, *Sci. Total Environ.* 424 (2012) 1–10.
- [14] L. Zhang, W. Wang, L. Zhou, H. Xu, *Small* 3 (2007) 1618–1625.
- [15] X.N. Li, R.K. Huang, Y.H. Hu, Y.J. Chen, W.J. Liu, R.S. Yuan, Z.H. Li, *Inorg. Chem.* 51 (2012) 6245–6250.
- [16] H. Fu, S. Zhang, T. Xu, Y. Zhu, J. Chen, *Environ. Sci. Technol.* 42 (2008) 2085–2091.
- [17] S. Zhu, T. Xu, H. Fu, J. Zhao, Y. Zhu, *Environ. Sci. Technol.* 41 (2007) 6234–6239.
- [18] H. Huang, K. Liu, K. Chen, Y. Zhang, Y. Zhang, S. Wang, *J. Phys. Chem. C* 118 (2014) 14379–14387.
- [19] J. Wang, L. Tang, G. Zeng, Y. Liu, Y. Zhou, Y. Deng, J. Wang, B. Peng, *ACS. Sustain. Chem. Eng.* 5 (2017) 1062–1072.
- [20] L.S. Zhang, K.H. Wong, H.Y. Yip, C. Hu, J.C. Yu, C.Y. Chan, P.K. Wong, *Environ. Sci. Technol.* 44 (2010) 1392–1398.
- [21] Y.G. Zhou, Y.F. Zhang, M.S. Lin, J.L. Long, Z.Z. Zhang, H.X. Lin, J.C.S. Wu, X.X. Wang, *Nat. Commun.* 6 (2015).
- [22] H. Li, X. He, Z. Kang, H. Huang, Y. Liu, J. Liu, S. Lian, C.H.A. Tsang, X. Yang, S.T. Lee, *Angew. Chem. Int. Ed.* 122 (2010) 4532–4536.
- [23] L. Tang, G.M. Zeng, G.L. Shen, Y.P. Li, Y. Zhang, D.L. Huang, *Environ. Sci. Technol.* 42 (2008) 1207–1212.
- [24] S.Y. Lim, W. Shen, Z. Gao, *Chem. Soc. Rev.* 44 (2015) 362–381.
- [25] H. Dong, G. Zeng, L. Tang, C. Fan, C. Zhang, X. He, Y. He, *Water Res.* 79 (2015) 128–146.
- [26] J.L. Gong, B. Wang, G.M. Zeng, C.P. Yang, C.G. Niu, Q.Y. Niu, W.J. Zhou, Y. Liang, *J. Hazard. Mater.* 164 (2009) 1517–1522.
- [27] H. Zhang, H. Huang, H. Ming, H. Li, L. Zhang, Y. Liu, Z. Kang, *J. Mater. Chem.* 22 (2012) 10501–10506.
- [28] P. Mirtchev, E.J. Henderson, N. Soheilnia, C.M. Yip, G.A. Ozin, *J. Mater. Chem.* 22 (2012) 1265–1269.
- [29] F. Nan, Z. Kang, J. Wang, M. Shen, L. Fang, *Appl. Phys. Lett.* 106 (2015) 153901.
- [30] X. Wu, J. Zhao, S. Guo, L. Wang, W. Shi, H. Huang, Y. Liu, Z. Kang, *Nanoscale* 8 (2016) 17314–17321.
- [31] J. Tian, Y. Leng, Z. Zhao, Y. Xia, Y. Sang, P. Hao, J. Zhan, M. Li, H. Liu, *Nano Energy* 11 (2015) 419–427.
- [32] D. Yan, Y. Liu, C.Y. Liu, Z.Y. Zhang, S.D. Nie, *RSC Adv.* 6 (2016) 14306–14313.
- [33] J. Liu, Y. Liu, N. Liu, Y. Han, X. Zhang, H. Huang, Y. Lifshitz, S.-T. Lee, J. Zhong, Z. Kang, *Science* 347 (2015) 970–974.
- [34] H. Wang, X. Yuan, H. Wang, X. Chen, Z. Wu, L. Jiang, W. Xiong, G. Zeng, *Appl. Catal. B: Environ.* 193 (2016) 36–46.
- [35] H. Li, R. Liu, Y. Liu, H. Huang, H. Yu, H. Ming, S. Lian, S.T. Lee, Z. Kang, *J. Mater. Chem.* 22 (2012) 17470–17475.
- [36] X.J. Hu, J.S. Wang, Y.G. Liu, X. Li, G.M. Zeng, Z.L. Bao, X.X. Zeng, A.W. Chen, F. Long, *J. Hazard. Mater.* 185 (2011) 306–314.
- [37] L. Tang, H. Peng, J. Tang, G. Zeng, Y. Deng, J. Wang, Y. Liu, Y. Zhou, *Water Res.* 117 (2017) 175–186.
- [38] S. Zhu, Q. Meng, L. Wang, J. Zhang, Y. Song, H. Jin, K. Zhang, H. Sun, H. Wang, B. Yang, *Angew. Chem. Int. Ed.* 52 (2013) 3953–3957.
- [39] L. Zhang, H. Wang, Z. Chen, P.K. Wong, J. Liu, *Appl. Catal. B: Environ.* 106 (2011) 1–13.
- [40] J. Di, J. Xia, M. Ji, L. Xu, S. Yin, Z. Chen, H. Li, *J. Mater. Chem. A* 4 (2016) 5051–5061.
- [41] J. Yang, X. Wang, X. Zhao, J. Dai, S. Mo, *J. Phys. Chem. C* 119 (2015) 3068–3078.
- [42] F. Chen, Q. Yang, J. Sun, F. Yao, S. Wang, Y. Wang, X. Wang, X. Li, C. Niu, D. Wang, *ACS Appl. Mater. Interfaces* 8 (2016) 32887–32900.
- [43] X. Tu, S. Luo, G. Chen, J. Li, *Chem. A Eur. J.* 18 (2012) 14359–14366.
- [44] C. Li, G. Chen, J. Sun, Y. Feng, J. Liu, H. Dong, *Appl. Catal. B: Environ.* 163 (2015) 415–423.
- [45] X. Qian, D. Yue, Z. Tian, M. Reng, Y. Zhu, M. Kan, T. Zhang, Y. Zhao, *Appl. Catal. B: Environ.* 193 (2016) 16–21.
- [46] C. Zhang, C. Lai, G. Zeng, D. Huang, C. Yang, Y. Wang, Y. Zhou, M. Cheng, *Water Res.* 95 (2016) 103–112.
- [47] J. Di, J. Xia, Y. Ge, H. Li, H. Ji, H. Xu, Q. Zhang, H. Li, M. Li, *Appl. Catal. B: Environ.* 168 (2015) 51–61.
- [48] J. Di, J. Xia, M. Ji, H. Li, H. Xu, H. Li, R. Chen, *Nanoscale* 7 (2015) 11433–11443.
- [49] B. Halling-Sørensen, S. Nors Nielsen, P. Lanzky, F. Ingerslev, H. Holten Lützhøft, S. Jørgensen, *Chemosphere* 36 (1998) 357–393.
- [50] L.D. Chabalíná, M.R. Pastor, D.P. Rico, *Talanta* 115 (2013) 706–712.
- [51] L. Jørgensen, C.A. Stedmon, T. Kragh, S. Markager, M. Middelboe, M. Søndergaard, *Mar. Chem.* 126 (2011) 139–148.
- [52] H. Wang, X. Yuan, Y. Wu, G. Zeng, H. Dong, X. Chen, L. Leng, Z. Wu, L. Peng, *Appl. Catal. B: Environ.* 186 (2016) 19–29.
- [53] S. Valencia, J.M. Marín, G. Restrepo, F.H. Frimmel, *Water Res.* 51 (2014) 124–133.
- [54] C. Liu, L. Wang, Y. Tang, S. Luo, Y. Liu, S. Zhang, Y. Zeng, Y. Xu, *Appl. Catal. B: Environ.* 164 (2015) 1–9.
- [55] S. Gao, B. Gu, X. Jiao, Y. Sun, X. Zu, F. Yang, W. Zhu, C. Wang, Z. Feng, B. Ye, *J. Am. Chem. Soc.* 139 (2017) 3438–3445.
- [56] J. Wang, L. Tang, G. Zeng, Y. Deng, Y. Liu, L. Wang, Y. Zhou, Z. Guo, J. Wang, C. Zhang, *Appl. Catal. B: Environ.* 209 (2017) 285–294.
- [57] Y.C. Deng, L. Tang, G.M. Zeng, J.J. Wang, Y.Y. Zhou, J.J. Wang, J. Tang, Y. Liu, B. Peng, F. Chen, *J. Mol. Catal. A Chem.* 421 (2016) 209–221.
- [58] L. Tang, Y.C. Deng, G.M. Zeng, W. Hu, J.J. Wang, Y.Y. Zhou, J.J. Wang, J. Tang, W. Fang, *J. Alloys Compd.* 662 (2016) 516–527.